Evaluation of electrodeposited α-Mn_2O_3 as a catalyst for the oxygen evolution reaction

Moritz Kölbach[a,*], Sebastian Fiechter[a], Roel van de Krol[a], Peter Bogdanoff[a]

[a]*Institute for Solar Fuels, Helmholtz-Zentrum Berlin für Materialien und Energie GmbH, Hahn-Meitner-Platz 1, 14109 Berlin, Germany*

*Corresponding author
e-Mail: moritz.koelbach@helmholtz-berlin.de

Abstract

α-Mn_2O_3 is of interest as a low-cost and environmentally benign electrocatalyst for the Oxygen Evolution Reaction (OER) in the process of water splitting. Mechanically stable α-Mn_2O_3 electrodes are prepared by annealing of galvanostatically deposited $MnOOH_x$ layers on F:SnO_2-coated glass. The overpotential η to achieve a current density of j = 10 $mAcm^{-2}$ decreases from 590 to 340 mV with increasing layer thickness. Differential capacitance measurements reveal that this high OER activity can be attributed to the large electrochemically active surface area (ECSA), which scales linearly with the thickness of these highly porous and electrolyte-permeable films. The oxide layers exhibit a reversible oxidation behavior from Mn(III) ↔ Mn(IV). Although the intrinsic activity is small compared to that of other OER catalysts, such as $NiFeO_x$, the combination of high ECSA and good electrical conductivity of these α-Mn_2O_3 films ensures that high OER activities can be obtained. The films are found to be stable for >2 h in alkaline conditions, as long as the potential does not exceed the corrosion potential of 1.7 V vs. RHE. These findings show that α-Mn_2O_3 is a promising OER catalyst for water splitting devices.

Keywords: *Electrochemistry*, *Electrocatalysts*, *Water oxidation*, *Manganese*, *Electrodeposition*, *Solar fuels*

1. Introduction

The generation of hydrogen by solar-driven electrochemical water splitting is a promising approach to store renewable energies as a non-fossil fuel in large quantities. To achieve this goal, earth-abundant and highly active catalysts for both half reactions, the Hydrogen Evolution Reaction (HER) and the kinetically more challenging Oxygen Evolution Reaction (OER), have to be identified and developed for a mass market. These catalysts can be used in advanced electrolyzers, for example photoelectrochemical water splitting devices, by being deposited as co-catalysts on the surface or at the back contact of suitable photoelectrodes.

In nature, OER active catalysts are found in photosystem II which is located in the thylakoid membrane of the chloroplasts in the cells of plants and green algae. The catalytic center in this system consists of $CaMn_4O_5$-clusters embedded in a complex protein environment. In attempts to mimick this OER catalyst, metal oxides based on low-cost, earth-abundant and environmentally benign manganese compounds and complexes are being intensely studied. This interest is caused by the wide gamut of different and stable oxidation states which manganese ions can adopt, ranging from Mn^{II} to Mn^{VII}, and in addition by its relatively fast redox kinetics. These properties also form the basis for the application of manganese oxides as anode material in recharcheable lithium ion batteries [1,2] and in supercapacitors [3]. Besides approaches to mimic the O_2-evolving center in PS II in metal organic complexes [4,5] , inorganic Ca-Mn-oxides and Mn-oxides have been successfully synthesized and tested with respect to their ability to act as efficient OER catalysts [6-16]. Among these manganese-based catalysts, α-Mn_2O_3 showed the most promising activity in alkaline solution. It is able to produce a current density of 10 $mAcm^{-2}$ at an overpotential of η = 360 mV in 1 M KOH [14]. α-Mn_2O_3 can be synthesized via a simple and low-cost galvanostatic deposition on conductive substrates following a recipe for the preparation of MnO_2 layers [3]. In our modified process, amorphous $MnOOH_x$ is deposited from a solution containing Mn^{2+}-cations in a first step and afterwards annealed in air at 773 K to form crystalline α-Mn_2O_3 [17]. α-Mn_2O_3 possesses an orthorhombic crystal structure (space group P*cab*), in which Mn^{3+}-cations are octahedrally coordinated by O^{2-}-anions. These [MnO_6] octahedra are sharing corners and edges similar to the mineral bixbyite $(Fe_xMn_{1-x})_2O_3$ [18]. Due to the spin state $3d^3$ of Mn(III) in α-Mn_2O_3 highly distorted [MnO_6] octahedra are found in the lattice leading to a variety of different Mn-Mn and Mn-O distances which might beneficially influence the OER activity [18].

To prepare an OER active photoanode in a light-driven electrolysis device [19,20], the co-catalyst deposited on top of the light sensitive absorber has not only to be catalytically active, but also optically transparent in order to ensure that the incident light reaches the photoabsorber with negligible intensity losses. Since most catalysts are colored to some extent, the specific activity of the catalyst needs to be as high as possible. This demand is less stringent for catalysts used in electrolyzers, where optical transparency is not required.

In the literature, α-Mn_2O_3 and also other MnO_x phases were electrochemically deposited as porous films with different thicknesses [8,14,16]. McCrory et al. [21,22] described a benchmarking protocol to evaluate activity, stability, and Faradaic efficiency of electrodeposited OER catalysts. The primary figure of merit is the overpotential required to achieve a current density of 10 $mAcm^{-2}$. Moreover, turnover frequencies and specific activities can be calculated from the estimated electrochemical active surface area (ECSA) of

the electrodes enabling a meaningful comparison of different catalysts. In ref. [21] and [22] binary (e.g. CoO_x, NiO_x, IrO_x) and ternary (e.g. $CoFeO_x$, $Ni(Ce,Co,Cu,Fe,La)O_x$) electrocatalysts were investigated in acidic and alkaline electrolytes. The authors estimated the ECSA for each electrode material from the electrochemical double-layer capacitance C_d divided by the specific capacitance C_S of a smooth planar electrode surface of the same electrode material (see also eq. 1 below). Since the determination of C_S is difficult, a mean value of 40 µF cm^{-2} was used by them for all catalysts measured in 1 M NaOH. This value was derived from an extensive survey of literature data (see SI of [21,22]). The stability of the catalysts was evaluated by monitoring the change in overpotential needed to keep the current density constant at 10 mA cm^{-2} after two hours of operation. The electrodes were rotated with 1600 rpm to get rid of the O_2 formed at the surface, which could otherwise block the parts of the electrode area.

In this work we determine for the first time the specific activity of highly porous α-Mn_2O_3 layers and compare this result with other metal oxide OER catalysts. To this end, α-Mn_2O_3 of different film thicknesses are electrochemically deposited on conductive FTO glass substrates and characterized by cyclic voltammetry (CV) to determine their ECSA and their activity towards the OER. The morphology, crystal structure, optical properties, and stability of the films were also investigated. Despite the modest intrinsic OER activity of α-Mn_2O_3, a surprisingly low overpotential of 340 mV is needed to generate a current density of 10 $mAcm^2$. We will explain the origin of this high OER activity, and discuss the potential application and limitations for these electrodeposited α-Mn_2O_3 films in practical water splitting devices.

2. Experimental Section

Materials: $MnSO_4 \cdot H_2O$ (≥ 98 %), K_2SO_4 (≥ 98 %), $NiSO_4 \cdot 6\ H_2O$ (≥ 98 %) were obtained from Sigma-Aldrich and 1 M KOH solution from Merck. Conductive glass substrates (F:SnO_2/glass, TEC 7) were purchased from Pilkington and cleaned in an ultrasonic bath in acetone (Sigma-Aldrich, 98 %) for 10 min, rinsed with demineralized water and dried under air.

Film Preparation: α-Mn_2O_3-films were deposited on FTO (1 x 1.3 cm^2) by galvanostatic deposition at a current density of 0.25 $mAcm^{-2}$ in an electrochemical glass cell with a three electrode arrangement, consisting of an Ag/AgCl-reference-electrode (+ 0.199 V vs. NHE) and a commercial coiled platinum wire as a counter electrode. The deposition was carried out in a solution of 0.5 M $MnSO_4$ and 0.5 M K_2SO_4 (pH ≈ 5.5) using a VersaSTAT 3 potentio-stat from Princeton Applied Research. Afterwards the films were thoroughly rinsed with

demineralized water and dried in air. In order to obtain the crystalline α-Mn_2O_3 phase, the samples were annealed at 773 K in air for 1 h.

Electrochemical measurements: Evaluation of the OER-activity of the films was performed using cyclic voltammetry measurements in an electrochemical cell with a three-electrode arrangement consisting of an Ag/AgCl-reference-electrode (+ 0.199 V vs. NHE), a commercial coiled platinum electrode as counter electrode and the respective deposited films as working electrode. The potential of the working electrode was controlled with a Versastat 3 potentiostat from Princeton Applied Research. The evaluation of the OER activity of the films was conducted in 1 M KOH with a sweep rate of 5 mV/s directly after a potentiostatic pre-oxidation step at a potential of 1.45 V vs. RHE for t = 0.5 h. The measurements were manually corrected for iR-drop after measuring the total cell resistance with an impedance measurement from 100 kHz to 10 Hz with an amplitude of 10 mV at the open-circuit potential.

Galvanostatic stability measurements of the films were performed at a current density of j = 10 $mAcm^{-2}$ for t = 2 h in 1 M KOH with a three-electrode arrangement using an Ag/AgCl reference electrode, a coiled platinum wire as a counter electrode and a rotating working electrode (~ 400 rpm). The rotation axis was in line with the substrate plane. The measured potential was again corrected for the iR-drop, as described above.

The differential capacitance C_d of the α-Mn_2O_3 films was determined by fast potential sweep curves in a potential range from 1.2 – 1.3 V vs. RHE, where the Faradaic currents are negligible. The electrolyte was 1 M KOH, the sweep rates varied from 10 – 50 mV/s.

All potentials were referred to RHE calculated from the experimental potential $E_{measured}$, the potential of the reference electrode $E_{Ag/AgCl} = +0.199\,V$ and the pH of the electrolyte solution according to the formula $E_{RHE} = E_{measured} + E_{Ag/AgCl} + 0{,}059 \cdot pH$. The overpotential η for the OER was determined using the equation $\eta = E_{RHE} - 1.23\,V$.

Structural and Morphological Characterization: XRD patterns of the α-Mn_2O_3 films were obtained with a Bruker D8 Advance diffractometer with a CuK_α (λ = 1.5406 Å) x-ray tube in Bragg−Brentano geometry and a Sol-X energy dispersive detector. The measurements were performed in the 2-theta angle range of 20° - 70° with a step size of 0.02° and an integration time of 10 s/step. Scanning electron microscopy (SEM) images were recorded using a LEO 1530 Gemini.

3. Results and discussion

3.1 Electrochemical deposition and film morphology

Amorphous $MnOOH_x$ films with different thicknesses were deposited onto conducting FTO substrates via galvanostatic deposition from a Mn^{2+} containing solution (deposited charge Q = 1 – 400 $mCcm^{-2}$). Figure S1a shows the current voltage curve of a FTO working-electrode immersed in the Mn^{2+} solution from which an onset of the deposition current at about E ≈ 1.1

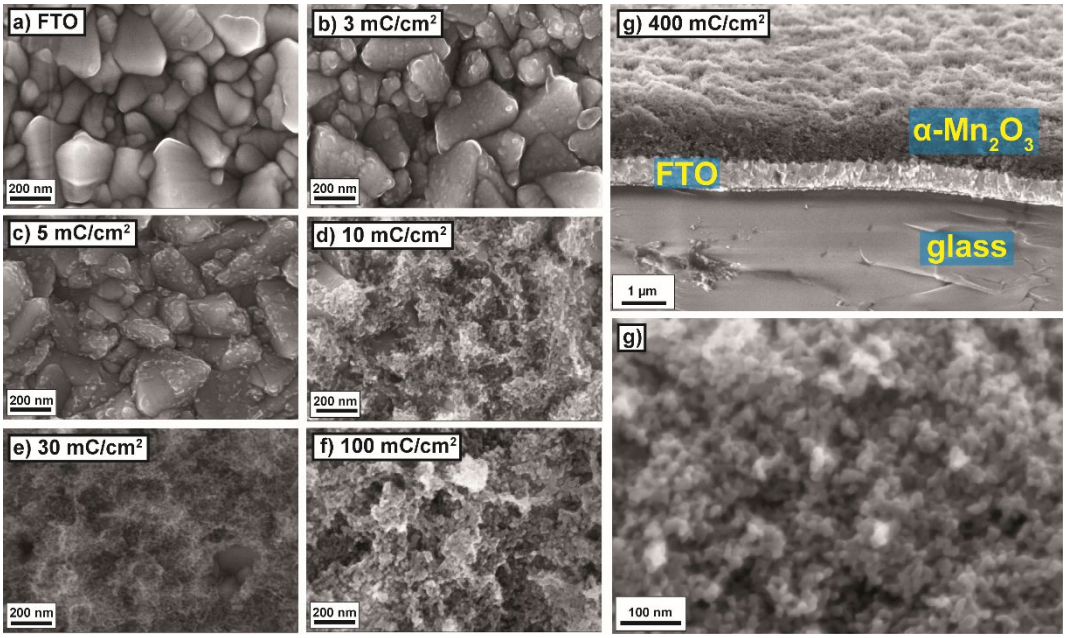

Fig. 1. Scanning electron micrographs of **a)** pristine FTO-glass substrate. **b)** and **c)** are showing α-Mn_2O_3 particles grown on top of the F:SnO_2 crystallites (edge length up to 50nm). In the micrographs **d)** – **f)** porous α-Mn_2O_3 films consisting of small particle sizes are shown. **g)** and **h)** Cross section micrographs of a layer deposited after a charge flow of 400 $mCcm^{-2}$. This highly porous layer of ~ 1 µm thickness consists of particles of about 20 nm in diameter.

V vs. RHE can be identified. The E-Q curve of the galvanostatic deposition process (Fig. S1b) shows a sharp increase of the potential E in the first two minutes, before a constant deposition potential E_D = 1.41 V is reached. Obviously, the growth mode changes as the deposition onto the FTO is energetically favored compared to the growth on an already formed $MnOOH_x$ seed layer. Within the applied potential range the current is exclusively caused by the oxidation of Mn^{2+}, resulting in the formation of a $MnOOH_x$ film. The OER activity of both the FTO substrate as well as the formed $MnOOH_x$ layers are negligible small at pH 5. The constant deposition potential indicates that the resistivity of the deposited layer is significantly lower than that of the employed FTO substrates (~ 10 Ω/□). If this were not the case, the internal ohmic drop within the deposited layer would lead to a continuously increasing deposition potential in order to maintain the fixed current density of 0.25 $mAcm^{-2}$.

Figure S2 shows the obtained electrodes after the final annealing step at 773 K for 1h in air. In the XRD diffractograms (Fig. S3) of these films, diffraction lines of the α-Mn_2O_3 crystal phase are visible for electrodes with a deposited charge of at least 100 mCcm^{-2}. For smaller loadings, the XRD patterns only show the reflections of FTO because of the small amount of α-Mn_2O_3 deposited.

The morphology of the annealed samples was studied by SEM analysis as shown in Figs. 1a-h. The deposition of small amounts (< 5 mCcm^{-2}) of $MnOOH_x$ leads to the formation of separated α-Mn_2O_3 crystallites that are randomly distributed over the FTO-substrate. These crystallites have edge lengths of up to 50 nm (Figs. 1a–c). As soon as the deposition charge Q exceeds 10 mCcm^{-2}, the structure of the annealed films changes and shows homogeneous and highly porous layers now fully covering the substrate. Figures 1.g-h show cross sections of the thickest layer (400 mCcm^{-2}) at different magnifications after annealing. The α-Mn_2O_3 film is highly porous and has a thickness of about 1 µm. The particles in the film have a diameter of ~ 20 nm, a value also confirmed by applying Scherrer´s equation to the full-width at half-maximum (FWHM) of the α-Mn_2O_3 <211> reflection (k = 0.94, λ = 1.5406 Å) (Fig. S3). From this, a mean crystallite size of 17 nm was obtained.

One objective of our contribution is the determination of the specific OER activity of the electrodeposited α-Mn_2O_3, which can be calculated from the current density and the real accessible ECSA of the electrodes. In a first step, the differential capacitance (C_d) of the porous electrodes was measured. The C_d is proportional to the ECSA under the reasonable assumption that all the electrodes consists of α-Mn_2O_3 and therefore have the same specific capacitance C_s.

To determine C_d, cyclic voltamograms were recorded in 1 M KOH with scan rates from 10 – 50 mVs^{-1} in a potential range between 1.2 and 1.3 V vs. RHE. The results are shown in Fig. S4a for a α-Mn_2O_3 electrode deposited using a charge of 400 mCcm^{-2}. Since the very first CV curve always showed a non-negligible Faradaic contribution to the oxidation current, we only show curves that are repeatable (usually from the second sweep onward). The linear increase of the plateau current densities with scan rate clearly indicates charging and discharging of the Helmholtz double layer. It has to be noted that the measured current is also expected to include a pseudocapacitance contribution, which is caused by fast and reversible superficial redox reactions. Such pseudocapacitances are typical for Mn oxide-based electrodes [23,24]. However, this is also proportional to the ECSA.

The differential capacitance can be calculated from the slope of the current density vs. scan rate (Fig. S4b) using the following equation [21,22]:

$$j_c = C_d \cdot \frac{d\varphi}{dt} \qquad \text{Eq. (1)}$$

Fig. 2 (left y-axis) shows the differential capacitance C_d of all annealed films, determined at a potential of 1.25 V vs. RHE, as a function of the charge Q used to deposit the films. The curve reveals a nearly linear relationship over the whole range. This implies that the electrochemical accessible surface area is proportional to the amount of deposited material. This is only possible if the porosity of the films is homogeneous, and if the Mn oxide particles have a uniform particle size that does not depend on the film thickness. This is indeed consistent with what we observe in the SEM images of Fig. 1. Moreover, the linear relationship even holds

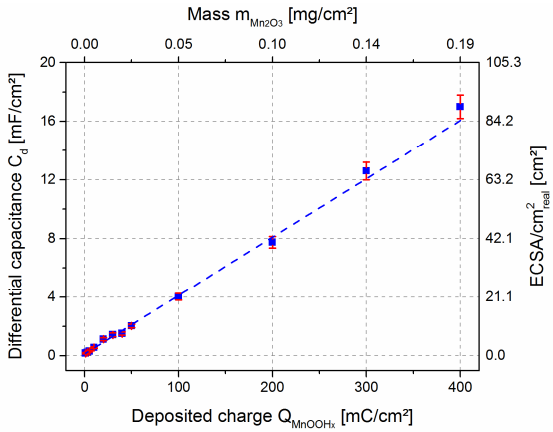

Fig. 2. Differential capacitance C_d of the annealed films as a function of charge Q used to deposit the $MnOOH_x$ films. The upper axis shows the estimated mass of the α-Mn_2O_3-electrodes (see text). The right axis depicts the estimated electrochemically active surface area (ECSA).

during the initial stages of growth, i.e., before a continuous manganese oxide layer is formed. This indicates that the ECSA rapidly increases with the amount of deposited manganese oxide and that the contribution to the capacitance of the underlying FTO to the total ECSA is negligible even for the thinnest (non-continuous) films. Finally, the results show that the electrolyte has access to all parts of the porous electrode layers, which is an important requirement for highly efficient thin film OER catalysts.

3.2 Estimation of the ECSA

To compare different electrocatalysts, their specific activity is an important descriptor which has been, until recently, often neglected in literature. This might be due to the issue that the actual electrochemically active surface area (ECSA) of the investigated electrode is needed to calculate the specific activity. One way to estimate the ECSA is the conversion of the differential capacitance C_d of the electrode following the description also used by McCrory et al. [21,22]:

$$ECSA = \frac{C_d}{C_s} \qquad \text{Eq. (2)}$$

Here C_s is the specific capacitance of the considered material. In general, C_s can be determined by a capacitance measurement of a well-known area of a smooth and planar electrode surface measured under the same experimental conditions. Unfortunately, the specific capacitance C_s is difficult to determine experimentally since most films show significant roughness and a range of surface orientations.

McCrory et al. [21] compared the specific activities of several OER-catalysts under the assumption that all catalysts can be described by an averaged unique specific capacitance of C_s = 0.04 mFcm^{-2} inferred from values reported in the literature (see SI of ref. [21]), measured in 1 M KOH or 1 M NaOH. Although this approach enables a comparison of different materials it is a simplification for metal oxides because metal oxides of different composition, crystal structure and morphology can provide a broad range of specific capacitances [25].

To determine the value of C_s more specifically for our α-Mn_2O_3 electrodes measured in 1 M KOH, a dense crystalline α-Mn_2O_3 film was prepared by reactive magnetron sputtering on an FTO substrate [26]. A roughness of R ≥ 1.9 ± 0.6 was estimated for these films from analysis of the scanning electron micrographs, as described in the supplemental information (Fig. S7). Combined with the measured capacitance C_d = (0.37 ± 0.03) mFcm^{-2}, the specific capacitance C_s of α-Mn_2O_3 is calculated to be $C_{S(\alpha\text{-}Mn_2O_3)}$ = (0.19 ± 0.08) mFcm^{-2}.

This value is close to the specific capacitance recently determined from an atomically planar α-Mn_2O_3 film deposited by Atomic Layer Deposition (ALD) onto silicon ($C_{S(Mn_2O_3)}$ = (0.17 ± 0.02) mFcm^{-2}) in our group. It should be noted that the differential capacitance estimated in this work is five times higher than the average value of McCrory et al. [20]. Nevertheless, this rather high specific capacitance is reasonable because manganese oxides are known to have high pseudocapacitances and are therefore considered as electrochemical super-capacitors [3,23,24].

We used $C_{S(Mn_2O_3)}$ to convert the measured differential capacitance C_d of our electrodeposited porous electrodes into an estimated ECSA per geometric cm² using Eq. (2). The right y-axis in Fig. 2 shows the calculated ECSA as a function of the amount of charge used to electrodeposit the catalyst film. It should be noted that these values can only be considered as a rough estimation due to the error-prone determination of the specific capacitance of α-Mn_2O_3. For comparison, also McCrory et al. assumed the error in the accuracy of their estimated ECSA values as large as one order of magnitude [22].

The upper axis in Fig. 2 shows the conversion of the deposited amount of $MnOOH_x$ into the deposited mass of α-Mn_2O_3. Since the average oxidation state of manganese in the as-deposited amorphous $MnOOH_x$-films is not known at this stage, a direct conversion of the consumed charge into the deposited mass of Mn_2O_3 is not possible. Therefore, nine Mn_2O_3-electrodes with a deposited charge of 400 $mCcm^{-2}$ were weighed after annealing and the mass of the FTO/glass substrate was subtracted. The mean value of the deposited mass is m = (0.19 ± 0.02) $mgcm^{-2}$. From this, it is possible to estimate the deposited masses of samples with different thicknesses by interpolation. Based on the mass deposited and the charge consumed during electrodeposition, the average oxidation state in the as-deposited amorphous $MnOOH_x$ is estimated to be about 3.7.

From the deposited mass, the density of α-Mn_2O_3 (4.5 g/cm^3) and the nominal film thickness d_{porous} ~ 1 µm estimated from the cross-sectional SEM image (Fig. S3), the porosity of the film can be calculated. A porosity of ~ 58% was obtained using following equation:

$$Porosity = 1 - \frac{d_{dense}}{d_{porous}} \qquad \text{Eq. (3)}$$

3.3 Oxygen Evolution Reaction (OER) activity

Current-voltage curves of all α-Mn_2O_3 electrodes, deposited with different deposition charges Q, were measured in a 1 M KOH electrolyte. In the beginning of each CV measurement, the cell resistivity was determined by impedance spectroscopy for each electrode. The resistivity of 12-15 Ω was almost the same for all experiments and therefore independent of the electrode layer thickness. This implies that the conductivity of the catalyst layer is much larger than the combined resistivity of the electrolyte and the FTO substrate. The current-voltage curves shown in Fig. 3 were all iR-corrected using the measured resistivity values. Furthermore, the current densities were corrected for the capacitive currents J_C, which were calculated from the differential capacitances of the respective films (see Fig. 2) using Eq. (1).

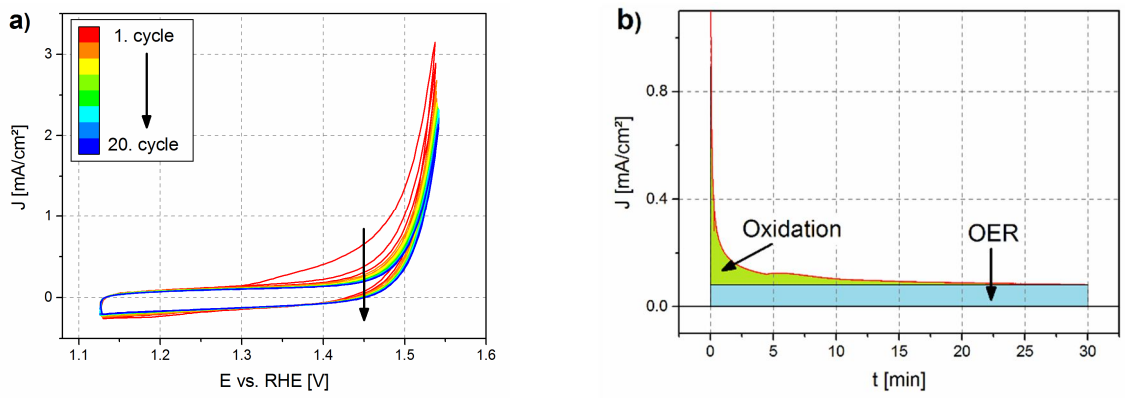

Figure 3. a) Cyclic voltammetry curves of an α-Mn_2O_3 (400 $mCcm^{-2}$) layer measured in 1 M KOH in the potential range from 1.125 – 1.525 V vs. RHE (20 cycles; scan rate: 5 mVs^{-1}) **b)** Potentiostatic measurement of the same electrode oxidized at a potential E = 1.45 V (RHE) for 30 min. The green area is interpreted as the charge necessary to partially oxidize Mn(III) to Mn(IV) in the porous film. The blue area is interpreted as the OER process additionally running in the background.

The shape of the current voltage curves in the first scan shows that more than one electrochemical process is occurring at the electrode (see Fig. S5a). This becomes particularly clear when looking at the corresponding Tafel plots, which reveal two linear ranges that can be assigned to two different electrochemical processes (see Fig. S5b). The slope of the Tafel curve in the OER range (η > 0.3V) was estimated to ~ 70 mV/decade whereas the oxidation process before the onset of the OER activity is characterized by a Tafel slope of ~ 300 mV/dec. However, the determination of these Tafel slopes are somewhat ambiguous owing to partial overlap of both oxidation processes. The process at η < 0.3 V is attributed to a partial oxidation of Mn(III) to Mn(IV) as already described in our previous work using XPS analysis of electrochemically treated samples [14]. However, all formed $Mn^{IV}O_2$ phases have a crystal structure different from α-Mn_2O_3, which crystallizes in the bixbyite lattice. This oxidation process is therefore connected with a comparable slow reconstructive phase transformation which probably limits the overall kinetic of the electrochemical current. This could explain the relatively high Tafel slope of ~ 300 mV/dec for this oxidation process (see Fig. S5b).

In order to exclusively study the OER activity of the electrodes, this first oxidation step in the manganese oxide films should be complete before the OER activity can be investigated. Fig. 3a shows the first 20 CV cycles measured in the range from 1.125 – 1.525 V vs. RHE of an α-Mn_2O_3 electrode (Q = 400 $mCcm^{-2}$) in 1 M KOH. In this potential range, the contribution of the first oxidation process to the total current decreases with the number of cycles. The curves in Fig. 3a show that the most pronounced change in the total current occurs at 1.45 V vs. RHE. Thus, we performed an electrochemical pre-oxidation at E = 1.45 V (RHE) for 30 min to reduce the contribution of the first oxidation step. The corresponding current transient of this process for the same α-Mn_2O_3 electrode (400$mCcm^{-2}$) is depicted in Fig. 3b.

The fast decreasing current spike at the very beginning of the measurement (time domain of a few seconds) is attributed to capacitive currents (Helmholtz double layer and fast pseudocapacitance reactions). From the capacitance of the electrode and the series resistance, it can be calculated that this charging process is ~ 95% complete after 1s. After the charging of the electrode the slower oxidation process of the α-Mn_2O_3 electrode can be observed. After about 15 min, the pre-oxidation process seems to be completed and the current density reaches a stationary value, which is attributed to the OER. It was calculated

that the green area shown in Fig. 3b has a value ~ 55 $mCcm^{-2}$, which is exclusively responsible for the oxidation of Mn^{III} to Mn^{IV} and does not include the initial charging of the Helmholtz layer. Using the related mass value shown in Fig. 2, the charge that has to flow to totally oxidize the manganese in this layer from Mn(III) to Mn(IV) can be estimated to amount to ~ 230 $mCcm^{-2}$. Assuming that the particles in the layer are spherical and have a uniform diameter of 17 nm, the measured charge corresponds to the oxidation of all manganese ions from +3 to +4 in shell of about 0.8 nm thickness. This corresponds to about four Mn-O monolayers in the spherical α-Mn_2O_3 particles [18]. Jaramillo et al. also described a α-Mn_2O_3 oxidation process in 0.1 M KOH, attributed to a reversible redox current wave in their CVs. This wave was, however, located at a more negative potential of about 1 V vs. RHE [16]. After reducing our α-Mn_2O_3 at a potential of 0.825 V vs. RHE for 30 min we are also able to observe this redox wave as shown in Fig. S6. Hence, it appears that α-Mn_2O_3 electrodes show two different reversible redox processes during the potential scan. One could speculate that the first step of oxidation at about 1 V vs. RHE is related to easier oxidable surface groups caused by a different ligand field of the manganese ions (oxygen vacancies or OH groups). The second process could then be due to the oxidation of bulk material in deeper layers close to the electrolyte interface. To what extent this pre-oxidation is a necessary precondition for the catalytic activity cannot be concluded from our experiments.

The potential sweeps recorded after 30 min. of pre-oxidation at 1.45 V vs. RHE are shown in Fig. 4a for a series of α-Mn_2O_3 electrodes with different thicknesses. The related Tafel plots are shown in Fig. 4b. In contrast to Fig. S5, these curves now only represent one dominant process, which is the OER. Electrochemical mass spectroscopy indeed confirms the evolution of oxygen during these experiments, with the oxygen mass signal showing an onset and slope that match well with those of the current (not shown).

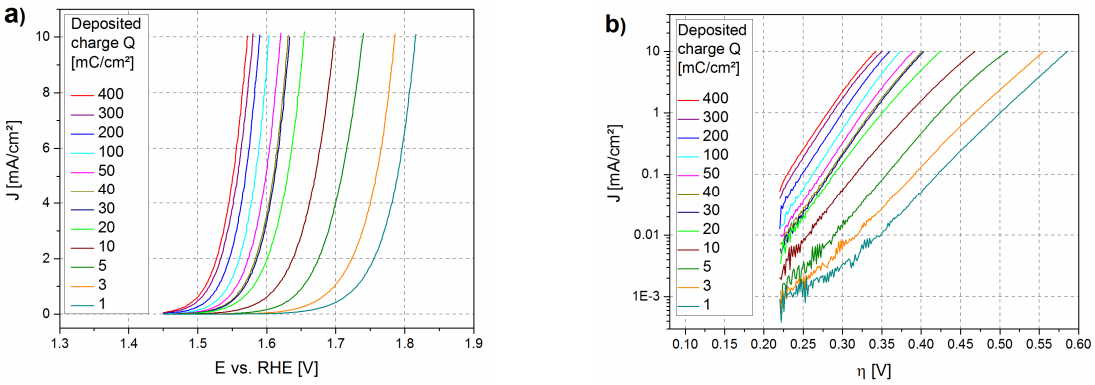

Fig. 4. a) Polarization curves of annealed and pre-oxidized (E = 1.45 V vs. RHE for 30 min) α-Mn_2O_3 films using different amounts of deposited charge Q. All measurements were performed with a scan rate of 5 mVs^{-1} in 1 M KOH. The current densities are corrected for capacitive charging currents and iR losses. b) Corresponding Tafel plots of the polarization curves shown in a).

For the thickest film (400 $mCcm^{-2}$), the required overpotential to achieve a current density of j = 10 $mAcm^{-2}$ is only 340 mV (iR-corrected). This is one of the lowest values ever reported for MnO_x-based catalysts, and comparable with other highly active catalysts for OER in alkaline conditions, such as $NiFeO_x$ [27]. Moreover, manganese is significantly more abundant, environmental benign and cheaper than nickel, which makes α-Mn_2O_3 a potentially attractive alternative to $NiFeO_x$.

Assuming that the OER mechanism and the ECSA-normalized electrode activities are identical in all electrodes, all Tafel plots in Fig. 4b should possess the same slope. In order to compare them, Tafel slopes of the electrodes of different thicknesses were determined in the current density range 0.1 - 1 $mAcm^{-2}$, since in this range the Tafel plots are almost perfectly linear. Figure S7 shows the slopes plotted as a function of the amount of charge used to electrodeposit the films. From this graph it is evident that electrodes deposited with a charge > 50 $mCcm^{-2}$ have the same Tafel slope of ~ 50 mV/dec. However, electrodes deposited using less charge show values of up to 80 mV/dec. A possible explanation for this behavior is the change of the morphology after annealing as a function of the deposited amount of $MnOOH_x$ (see Figs. 1a-f). For small amounts (Q < 5 $mCcm^{-2}$), the particles are characterized by facets of low Miller indices, whereas the spherical particles in the porous films (Q ≥ 10 $mCcm^{-2}$) are characterized by a higher number of facets of high Miller indices. These facets are expected to lead to more coordinatively unsaturated - and therefore more catalytically active - sites on the particles' surfaces (step and kink sites). As this thesis cannot be proved by our SEM images, high-resolution TEM analysis of the particles morphology is planned in forthcoming investigations using the technique described by Grothausmann et al. [28,29].

In order to compare the activity for the OER of the different electrodes the current densities at an overpotential of η = 280 mV and η = 350 mV were taken from the curves in Fig. 3 and plotted vs. the corresponding differential capacitance C_d, which is proportional to the ECSA (see Fig. 2). The results are shown in Figs. 5a-d. Under ideal conditions, a linear increase of the current density with the electrochemically accessible surface should be expected. Indeed, this behavior can be observed at electrodes with smaller loadings characterized by capacitances in the range from 0.3 to 2.0 $mFcm^{-2}$ (Figs. 5a and 5c). However, at higher loadings, and thereby increasing porosity of the layers, the current density deviates from the expected extrapolated line (Figs. 5b and 5d). Since the ohmic resistance of the films does not play a significant role (*vide supra*), we attribute this to diffusion limited mass transport in the electrolyte which leads to a local acidification within the porous electrode layers. Furthermore, evolved oxygen may block parts of the porous electrode area. These effects are especially significant for thick layers (indicated by large capacitances) and high current

densities. This explains why the deviation from the dashed line is larger for the higher overpotential η = 350mV (compare Figs. 5b,d).

At very low electrode loadings (< 0.3 $mFcm^{-2}$) also a deviation from the extrapolated line is evident as the current density increases only very moderately with capacitance (Fig 5a and 5c). This is again consistent with the lower intrinsic activities of the thinnest films, as discussed above.

Fig. 6 (left axis) shows the ECSA-normalized current densities of our electrodes at an overpotential of η = 350 mV. As explained above, the decrease below 50 $mCcm^{-2}$ is due to the lower intrinsic activity of the thinner films, while the deviation above 50 $mCcm^{-2}$ from the ideal blue dashed line (calculated with the extrapolation from Figs. 5c,d) is attributed to diffusion limitations. The resulting specific catalytic activity of our films is represented by the maximum

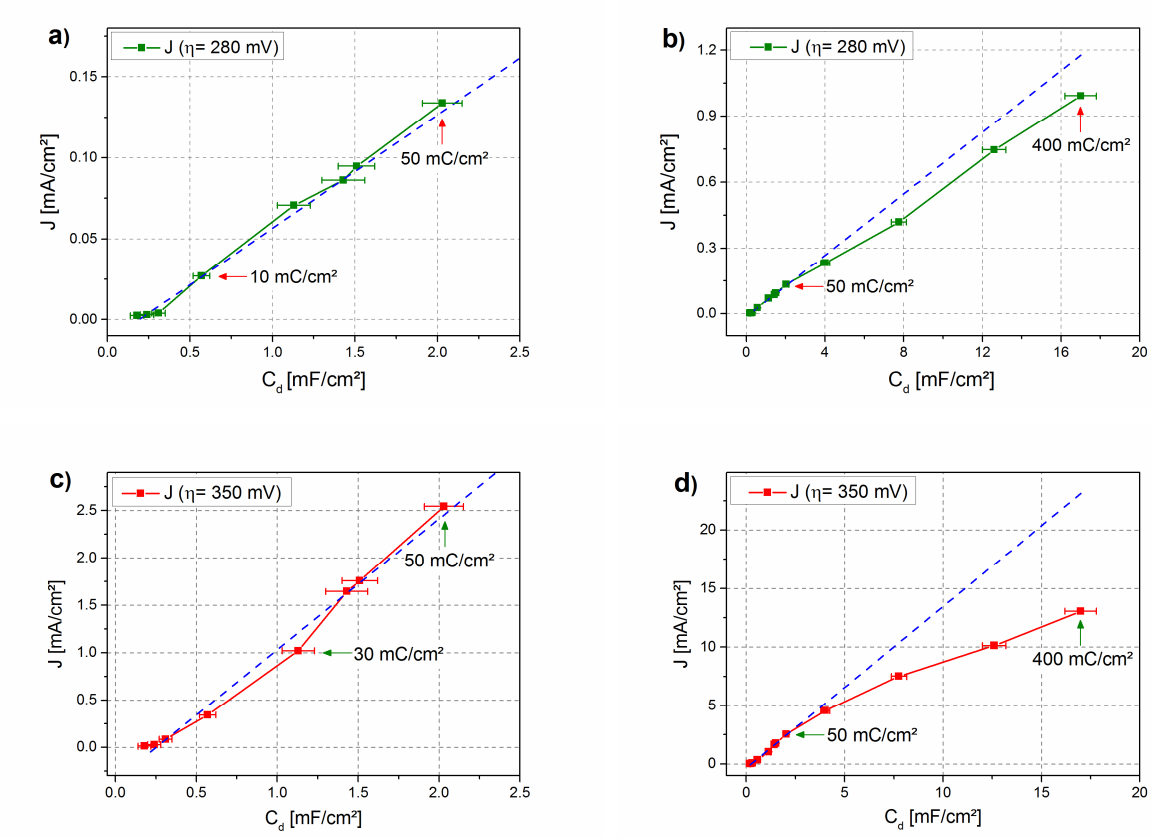

Fig. 5. Current density J [$mAcm^{-2}$] vs. differential capacitance C_d [$mFcm^{-2}$] of the α-Mn_2O_3 layers: Behavior of the electrodes at an overpotential η = 280 mV deposited a) with charges Q $\leq$ 50 $mCcm^{-2}$ and b) with charges $\leq$ 400 $mCcm^{-2}$. Corresponding curves for an overpotential η = 350 mV are shown in c) and d). The dashed lines are straight lines to guide the eye.

value of the curve, 0.24 $mAcm^{-2}$, calculated using $C_{S(\alpha\text{-}Mn_2O_3)}$ = 0.19 $mFcm^{-2}$. If we would instead use McCrory's value of 40 μFcm^{-2} for C_S, a specific activity of ~ 0.05 $mAcm^{-2}$ is estimated.

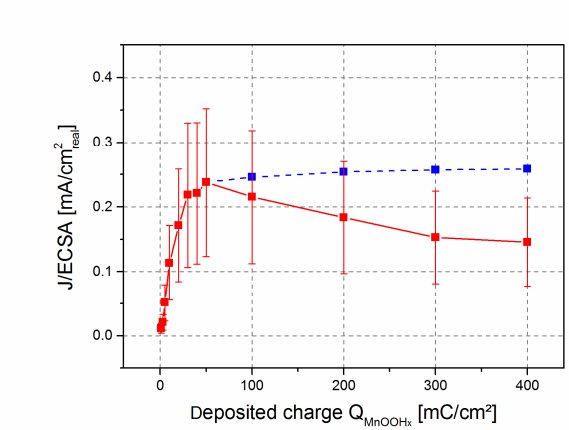

Fig. 6. J/(ECSA) of the of the α-Mn_2O_3 layers vs. the deposited charge Q using the specific capacitance as determined in this work (C_s = 0.19 ± 0.08 $mFcm^{-2}$).

In Table 1 the specific activities of different OER catalysts are summarized together with values of our Mn_2O_3 material. Compared to the well-known and highly active Ni containing catalysts, α-Mn_2O_3 has only a moderate specific OER activity. Despite this rather low value, very active films can be obtained by electrodeposition of thick porous layers with a large ECSA, a high electronic conductivity, and high electrolyte permeability.

Nevertheless, it has to be noted that the moderate specific activity of α-Mn_2O_3 prohibits the preparation of transparent and highly active films at the same time. This could be a showstopper for the use of this material as a co-catalyst on top of a photoanode under front illumination in an integrated light-driven electrolyzer (shadowing effects) [30]. For example, a 100 $mCcm^{-2}$ α-Mn_2O_3 layer would have to be deposited on a photoanode to catalyse the OER with a current densitiy of j = 5 $mAcm^{-2}$ at an overpotential of η = 350 mV. However, UV-vis measurements showed that such a film only transmits ~ 64 % of the AM1.5 solar spectrum, which could be absorbed by a photoanode with a bandgap of 1.8 eV. This is clearly a non-tolerable loss of efficiency. However, for application as a catalyst on the backcontact of a photoelectrode in superstrate geometry [31], highly porous α-Mn_2O_3 electrodes could be a promising and cheap alternative to noble metal—and even nickel—based catalysts.

Besides the specific activity (current density / ECSA; see Fig. 5), the specific mass activity (current density / mass) could also be used to benchmark OER catalysts with regard to their material utilization. Fig S9 shows the specific mass activity of the α-Mn_2O_3 electrodes as a function of the deposited charge at an overpotential of η = 350 mV. Due to the nearly linear

relationship of the mass and the ECSA of the films, the shape of the curve is similar to the one of the specific activity (see Fig. 5). In the maximum of the curve (Q = 20 – 50 $mCcm^{-2}$), the specific mass activity is j_{mass} ~ 110 A/g.

Table 1. Specific catalytic activity (ECSA) of different OER catalysts determined according to McCrory et al. [22].

OER catalyst	Specific activity η = 350 mV [$mAcm^{-2}_{real}$]
α-Mn_2O_3	~ 0.05 [a] ~ 0.24 [b]
NiCo	0.31 ± 0.21[a]
CoFe	0.53 ± 0.24[a]
NiMoFe	2.1 ± 1.4[a]
NiFe	2.78 ± 1.65[a]

[a] Results from McCrory, using C_s = 0.04 $mFcm^{-2}$
[b] results from this paper, using C_s = (0.19 ± 0.08) $mFcm^{-2}$.

3.4 Electrochemical stability of α-Mn_2O_3 electrodes under alkaline conditions

Besides the electrocatalytic activity, the electrochemical stability of the catalyst in the electrolyte is perhaps even more important for practical applications. Fig. 7 shows the galvanostatic stability of selected Mn_2O_3 electrodes of different thicknesses at a current density j = 10 $mAcm^{-2}$ measured for 2 h in 1 M KOH. The electrode was rotated using a rod as rotation axis which was perpendicularly fixed to the substrate at the back side of the electrode in its geometric center, in order to quickly remove the generated oxygen bubbles, which could block actives sites. Electrodes with a deposited mass-equivalent of 40 $mCcm^{-2}$ and 400 $mCcm^{-2}$ appear to be stable under the chosen measurement conditions. The voltage that has to be applied to keep the current density at 10 $mAcm^{-2}$ increases only very slightly. Electrodes with smaller loadings, however, show a pronounced increase of the required potential with time which indicates dissolution of the α-Mn_2O_3. The effect becomes more significant at lower loadings and, more importantly, more positive potentials.

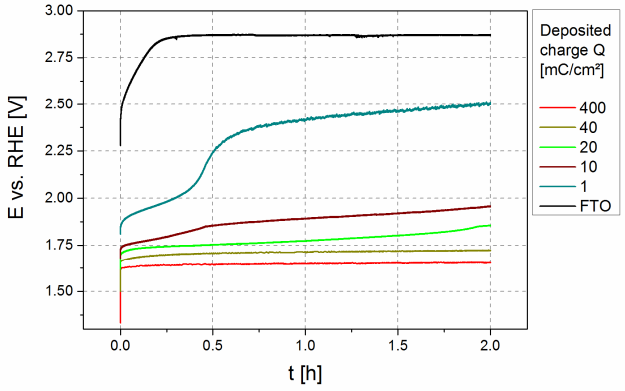

Figure 7. Galvanostatic stability measurements of rotated Mn_2O_3 electrodes deposited with different loadings and recorded at a current density of 10 $mAcm^{-2}$ in 1 M KOH. Best stabilities were obtained with layers deposited with Q ≥ 40 $mCcm^{-2}$.

From Fig. 7 it can be concluded that when the potential rises to values more positive than about 1.75 V corrosion processes become dominant. We indeed found that the appearance of the electrodes changes significantly if the potential exceeds 1.75 V during the electrochemical stability test. Thus, we conclude that α-Mn_2O_3 has a corrosion potential in the range of 1.7 - 1.75 V vs. RHE. From these results, we can derive an important design criterion for OER electrodes based on α-Mn_2O_3: the specific surface area of the electrode needs to be sufficiently high to ensure that the desired current density can be reached at potentials < 1.7 V vs. RHE.

4. Conclusion

It has been shown that highly porous α-Mn_2O_3 layers with large electrochemically active surface areas can be prepared by galvanostatic deposition from a Mn^{2+} solution. Layers of up to 1 µm thickness can be grown, which are composed of ~ 17 nm large nanoparticles and show nevertheless good electronic conductivity. After normalizing for the ECSA, an intrinsic activity of 0.24 $mAcm^{-2}_{real}$ for these α-Mn_2O_3 electrodes was obtained. Although this is a factor of ~ 60 smaller than for the best $NiFeO_x$ electrodes, current densities of 10 $mAcm^{-2}$ could be obtained at overpotentials as low as 340 mV for 1 µm thick films because of their high ECSA. The films are found to be stable for at least 2 h under alkaline conditions, provided the potential does not exceed the corrosion potential of 1.7 V vs. RHE. Since manganese is a cheap, abundant, and environmentally benign, and the preparation of OER active electrode layers is simple and scalable, it is a promising candidate for water spitting applications.

Acknowledgments

Part of this work was supported by the German Federal Ministry of Education and Research (BMBF project “MANGAN”, #03SF0505).

References

[1] M.M. Thackeray, Prog. Solid State Chem., 25 (1997) 1-71.
[2] M.-S. Wu, P.-C.J. Chiang, J.-T. Lee, J.-C. Lin, J. Phys. Chem. B, 109 (2005) 23279-23284.
[3] S. Devaraj, N. Munichandraiah, Electrochem. Solid-State Lett., 8 (2005) A373-A377.
[4] R. Brimblecombe, A. Koo, G.C. Dismukes, G.F. Swiegers, L. Spiccia, J. Am. Chem. Soc., 132 (2010) 2892-2894.
[5] R.K. Hocking, R. Brimblecombe, L.-Y. Chang, A. Singh, M.H. Cheah, C. Glover, W.H. Casey, L. Spiccia, Nat. Chem., 3 (2011) 461-466.
[6] A. Ramírez, P. Bogdanoff, D. Friedrich, S. Fiechter, Nano Energy, 1 (2012) 282-289.
[7] M. Wiechen, I. Zaharieva, H. Dau, P. Kurz, Chem. Sci., 3 (2012) 2330-2339.
[8] Y. Gorlin, B. Lassalle-Kaiser, J.D. Benck, S. Gul, S.M. Webb, V.K. Yachandra, J. Yano, T.F. Jaramillo, J. Am. Chem. Soc., 135 (2013) 8525-8534.
[9] D.M. Robinson, Y.B. Go, M. Mui, G. Gardner, Z. Zhang, D. Mastrogiovanni, E. Garfunkel, J. Li, M. Greenblatt, G.C. Dismukes, J. Am. Chem. Soc., 135 (2013) 3494-3501.
[10] M. Huynh, D.K. Bediako, Y. Liu, D.G. Nocera, J. Phys. Chem. C, 118 (2014) 17142-17152.

[11] M. Fekete, R.K. Hocking, S.L.Y. Chang, C. Italiano, A.F. Patti, F. Arena, L. Spiccia, Energy Environ. Sci., 6 (2013) 2222-2232.
[12] M. Huynh, D.K. Bediako, D.G. Nocera, J. Am. Chem. Soc., 136 (2014) 6002-6010.
[13] C.E. Frey, M. Wiechen, P. Kurz, Dalton Trans., 43 (2014) 4370-4379.
[14] A. Ramírez, P. Hillebrand, D. Stellmach, M.M. May, P. Bogdanoff, S. Fiechter, J. Phys. Chem. C, 118 (2014) 14073-14081.
[15] M. Huynh, C. Shi, S.J.L. Billinge, D.G. Nocera, J. Am. Chem. Soc., 137 (2015) 14887-14904.
[16] Y. Gorlin, T.F. Jaramillo, ECS Trans., 41 (2011) 1701-1707.
[17] C. Wei, W. Ning, L. Li, C. Yanran, C. Xia, C. Quanjing, G. Lin, Nanotechnology, 20 (2009) 445601.
[18] S. Geller, Acta Crystallogr., Sect. B: Struct. Sci., Cryst. Eng. Mater., B27 (1971) 821-828.
[19] S. Fiechter, Photoelectrochemical Water Decomposition, in: D. Stolten, B. Emonts (Eds.), Hydrogen Science and Engineering - Materials, Processes, Systems and Technology, WILEY-VCH, 2016, pp. 441-495.
[20] S. Fiechter, Artificial Photosynthesis – An Inorganic Approach, in: B. Robert (Ed.), Artificial Photosynthesis, Elsevier, 2016, pp. 100-125.
[21] C.C.L. McCrory, S. Jung, J.C. Peters, T.F. Jaramillo, J. Am. Chem. Soc., 135 (2013) 16977-16987.
[22] C.C.L. McCrory, S. Jung, I.M. Ferrer, S.M. Chatman, J.C. Peters, T.F. Jaramillo, J. Am. Chem. Soc., 137 (2015) 4347-4357.
[23] Y.-S. Chen, C.-C. Hu, Y.-T. Wu, J. Solid State Electrochem., 8 (2004) 467-473.
[24] Y. Chen, J.-W. Wang, X.-C. Shi, B.-Z. Chen, Electrochim. Acta, 109 (2013) 678-683.
[25] C.D. Lokhande, D.P. Dubal, O.-S. Joo, Curr. Appl. Phys., 11 (2011) 255-270.
[26] A. Kratzig, PhD thesis, TU Berlin, 2015.
[27] D.A. Corrigan, J. Electrochem. Soc., 134 (1987) 377-384.
[28] R. Grothausmann, G. Zehl, I. Manke, S. Fiechter, P. Bogdanoff, I. Dorbandt, A. Kupsch, A. Lange, M.P. Hentschel, G. Schumacher, J. Banhart, J. Am. Chem. Soc., 133 (2011) 18161-18171.
[29] R. Grothausmann, S. Fiechter, R. Beare, G. Lehmann, H. Kropf, G.S. Vinod Kumar, I. Manke, J. Banhart, Ultramicroscopy, 122 (2012) 65-75.
[30] F.F. Abdi, L. Han, A.H.M. Smets, M. Zeman, B. Dam, R. van de Krol, Nat. Commun., 4 (2013) 2195.
[31] P. Bogdanoff, D. Stellmach, O. Gabriel, B. Stannowski, R. Schlatmann, R. van de Krol, S. Fiechter, Energy Technol., 4 (2016) 230-241.

Evaluation of electrodeposited α-Mn_2O_3 as a catalyst for the oxygen evolution reaction

Moritz Kölbach, Sebastian Fiechter, Roel van de Krol, Peter Bogdanoff

Supporting information

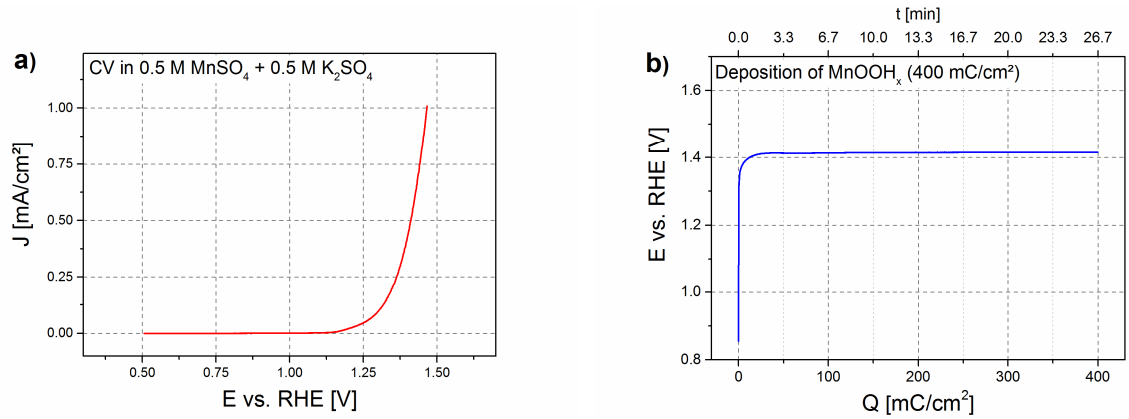

Fig. SI-1. a) Line scan of the first polarization curve for the deposition of a $MnOOH_x$ layer onto a FTO-glass substrate in a solution of 0.5 M $MnSO_4$ and 0.5 M K_2SO_4; scan rate: 5 mVs^{-1} **b)** Potential vs.

electrodeposition charge for galvanostatically deposited $MnOOH_x$ (Q = 400 mC/cm^2) in a solution of 0.5 M $MnSO_4$ and 0.5 M K_2SO_4; j = 0.25 mAcm^{-2}.

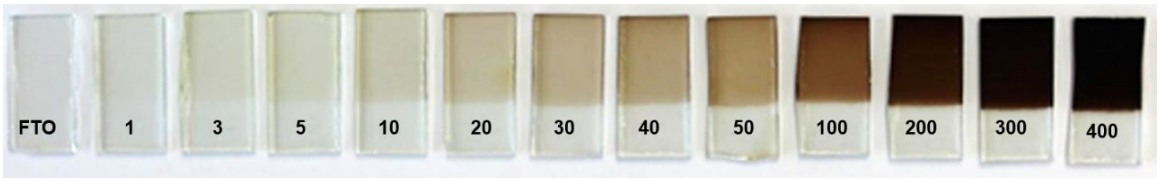

Fig. SI-2: α-Mn_2O_3 films obtained after a heat treatment at 773 K for 1h in air from amorphous layers deposited on FTO glass substrates varying the deposition charge Q (mCcm^{-2}) from 1 to 400 mCcm^{-2}.

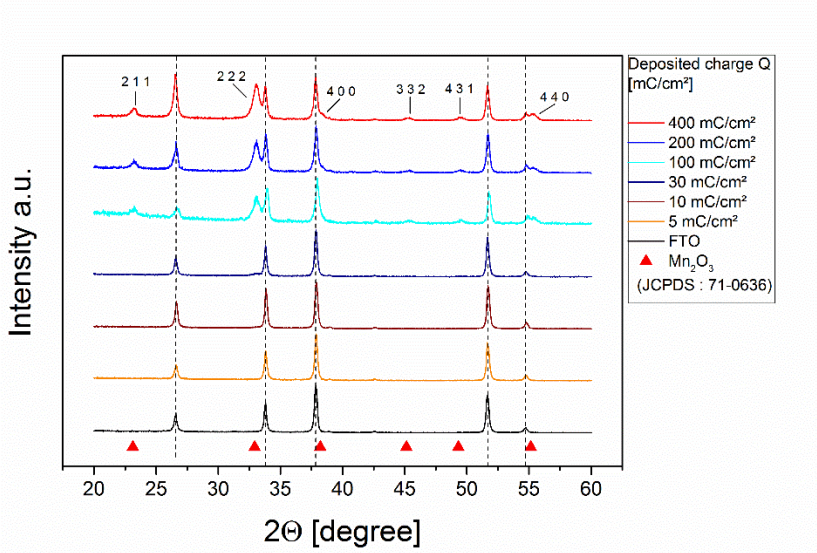

Fig. SI-3. X-ray diffraction patterns of $MnOOH_x$-films deposited onto FTO glass substrates after annealing at 773 K for 1h varying the deposited charge from 1 to 400 mC/cm². Crystalline α-Mn_2O_3 phase crystallizing in the distorted bixbyite structure (JCPDS 71-0636) are indexed in the figure. Diffraction lines become visible in the films when the charge used to deposit the films exceeds 100 mC/cm². For smaller loadings, the XRD patterns only show the reflections of FTO because of the insufficient amount of α-Mn_2O_3.

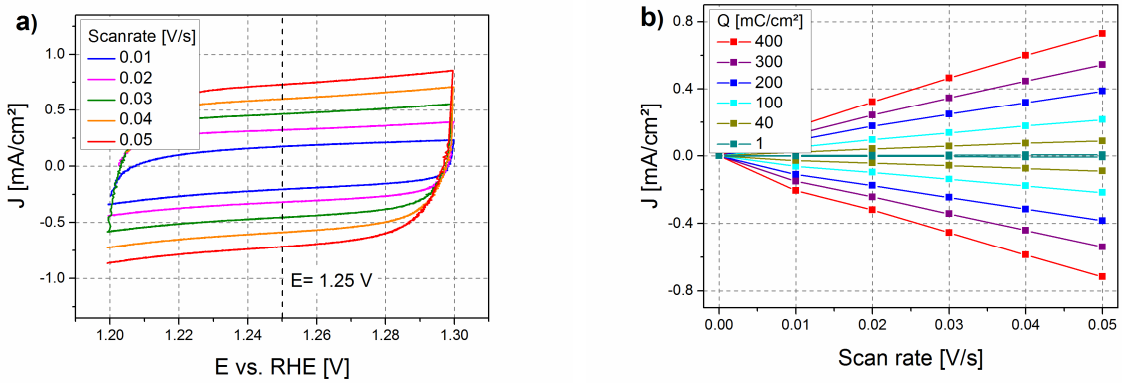

Figure SI-4. Determination of the differential capacitance C_d of Mn_2O_3 electrodes from cyclovoltammetric measurements in the potential range 1.2 – 1.3 V (RHE) as a function of scan rate using a 1 M KOH electrolyte **a)** CV curves of an α-Mn_2O_3 film deposited at 400 mC/cm^2 as a function of scan rate (0 – 0.05 V/s. **b)** Anodic and cathodic current density vs. scan rate at a potential E = 1.25 V for layers deposited by charge densities varied from 1 – 400 mC/cm^2.

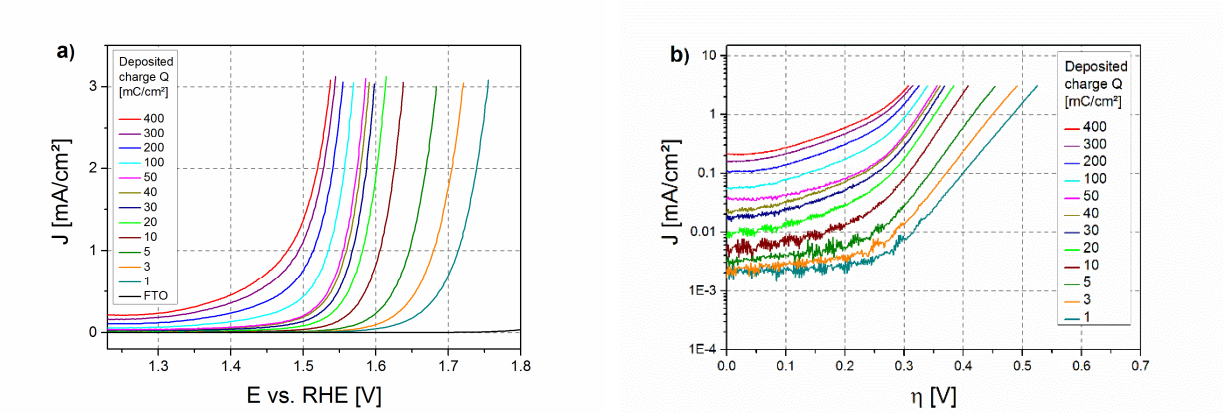

Figure SI-5. iR-corrected polarization curves of annealed (773 K for 1 h) α-Mn_2O_3 electrodes of different thicknesses (see Fig. SI-1), galvanostatically deposited using different deposition charges. All measurements were performed at a scan rate of 5 mV/s in 1 M KOH; only the first scans are shown. b) Corresponding Tafel plots.

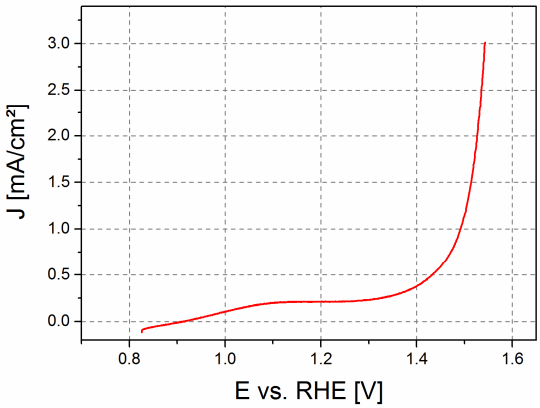

Figure SI-6. Polarization curve in 1 M KOH of an annealed (773 K for 1 h) α-Mn_2O_3 electrode, directly measured after applying a potential of E = 0.825 V vs. RHE for 30 min. The scan rate was 5 mVs^{-1}.

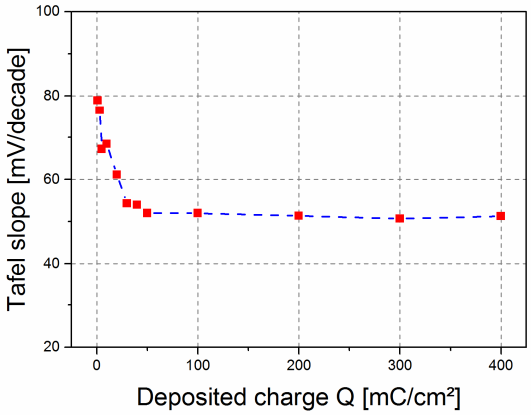

Figure SI-7. Tafel slope of the annealed α-Mn_2O_3 electrodes extracted from Fig. 3b as a function of deposited charge Q. The slope was determined in the current density range of 0.1 - 1 mA/cm^2. A constant value is observed for layers deposited with a charge ≥ 50 mC/cm^2 was found.

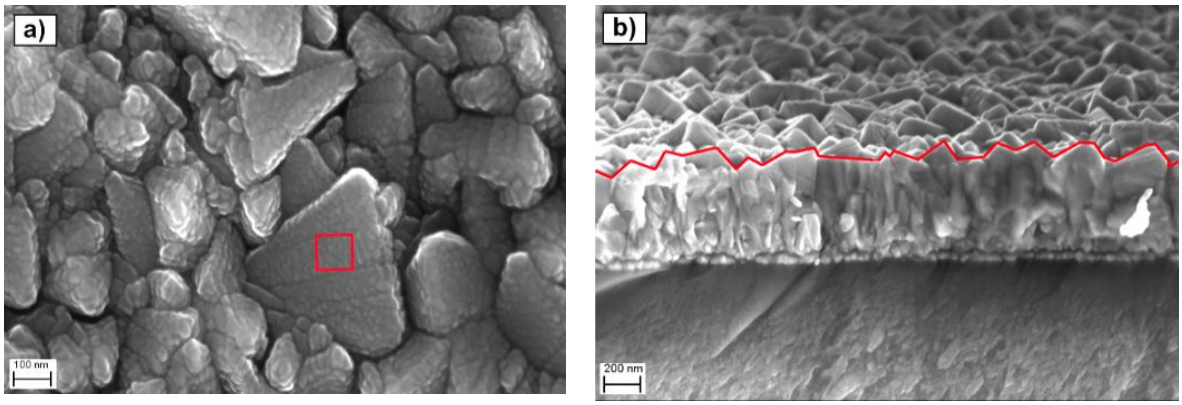

Figure SI-8. α-Mn_2O_3 film deposited by reactive magnetron sputtering on an FTO substrate. a.). Top view of the deposited film. Small facetted α-Mn_2O_3 crystallites are grown on top of larger FTO grains. b) Cross section view of the same layer. The length of red line was used to calculate the roughness of the FTO layer and the superimposed roughness of the Mn oxide particles.

To calculate the roughness factor of a flat α-Mn_2O_3 film (Fig. SI-8.a), deposited by sputtering, four cross sections were taken, the length of the red lines (Fig. SI-8.b) determined and squared. The mean value amounted to 1.6±0.2. A further increase of the roughness factor is given considering the ~ 15 nm size large Mn_2O_3 nanoparticles. Approximating their surface area by hemispheres, a radius r = 7.5 nm was assumed. An enlargement of the surface area by at least a factor of 1.9 ± 0.6 was calculated.

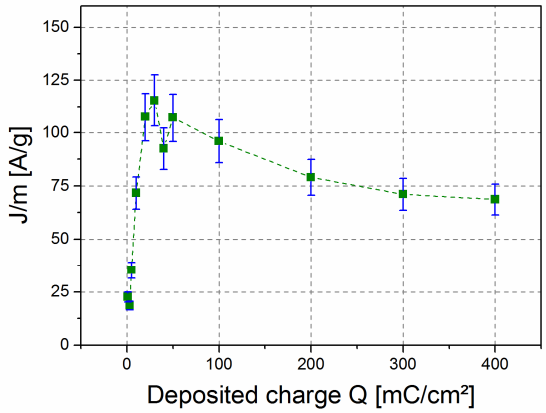

Fig. SI-9. Specifc mass activity of the α-Mn_2O_3 electrodes as a function of the deposited charge at an overpotential of η = 350 mV.